TRENDS IN SCIENCES 2026; 23(13): 14087
https://doi.org/10.48048/tis.2026.14087 RESEARCH ARTICLE

Effect of Mn and La Cation Substitution on the Structural and Magnetic Properties of Cobalt Ferrite Nanoparticles for Microwave Absorption Application

Suharno[1], Ramadona Rahmawati[2], Nurdiyantoro Putra Prasetya[3], Yana Taryana[4], Riyatun[2], Utari[2], Candra Kurniawan[5], Dede Djuhana[6], Terumitsu Tanaka[7] and Budi Purnama[2,*]

[1]Department of Physics Education, Faculty of Teacher Training and Education, Universitas Sebelas Maret, Surakarta 57126, Indonesia
[2]Department of Physics, Faculty of Mathematics and Natural Sciences, Universitas Sebelas Maret, Surakarta 57126, Indonesia
[3]Department of Physics, Faculty of Mathematics and Natural Sciences, Universitas Tanjungpura, Pontianak 78124, Indonesia
[4]Research Center for Telecommunication, National Research and Innovation Agency, Bandung 40135, Indonesia
[5]Research Center for Advanced Material, National Research and Innovation Agency (BRIN), KST BJ Habibie Office Area, Tangerang Selatan 15314, Indonesia
[6]Department of Physics, Faculty of Mathematics and Natural Sciences, Universitas Indonesia, Kampus Baru UI Depok, Jawa Barat 16424, Indonesia
[7]Department of Electronics, Kyushu University, Fukuoka 8190395, Japan

([*]Corresponding author's e-mail: bpurnama@mipa.uns.ac.id)

Received: 14 April 2026, Revised: 26 May 2026, Accepted: 5 June 2026, Published: 30 July 2026

Abstract

Cation engineering is a promising strategy for tuning the properties of cobalt ferrite ($CoFe_2O_4$)-based microwave absorbers. This work systematically studies the effects of Mn and La substitution on the high-frequency magnetic and dielectric properties of $CoFe_2O_4$ (CFO) within the X-band (8 - 12 GHz). X-ray diffractometer (XRD) analysis confirms that all synthesized nanoparticles retain an inverse-spinel face-centered cubic structure. Transmission electron microscopy (TEM) and selected area electron diffraction (SAED) results reveal nanostructures with average grain sizes increasing from 17.61 nm (pristine CFO) to 21.19 and 25.34 nm for Mn- and La-doped samples, respectively. Vibrating sample magnetometer (VSM) measurements show the saturation magnetization modifies from 52.33 to 61.10 emu/g (Mn-doped) and 13.60 emu/g (La-doped). Vector network analyzer (VNA) results indicate the electromagnetic wave absorption peak sharpens and shifts from 8.82 GHz to approximately 11.80 GHz for both doped samples. The doped CFO exhibits reduced real permeability (μ') and substantially increased imaginary permeability (μ''), yielding high magnetic loss tangents ($\tan \delta_m \approx 1.5$ - 1.6) and strong ferromagnetic resonance. Consequently, the doped samples demonstrate superior microwave absorption, with minimum reflection losses reaching approximately −18 dB for Mn-doped CFO and −15 dB for La-doped CFO. This study establishes a comprehensive structure-property-performance correlation, demonstrating that controlled cation substitution is a powerful method for designing high-performance X-band ferrite absorbers.

Keywords: Cobalt ferrite, Mn-doped, La-doped, Coprecipitation, Inverse spinel, Saturation magnetization, Microwave absorption

Introduction

The rapid advancement demand for high-frequency electronic devices, wireless communication systems, and radar technologies has intensified research into efficient microwave absorbing materials (MAMs) that can mitigate electromagnetic interference (EMI) within the X-band (8 - 12 GHz). Among various candidates, cobalt ferrite ($CoFe_2O_4$) nanoparticles have attracted considerable attention due to their superior magnetic-properties of high magnetic permeability, large magneto-crystalline anisotropy, as well as excellent chemical stability [1-8]. At the nano-order-scale, $CoFe_2O_4$ exhibits electromagnetic wave attenuation mechanisms dominated by magnetic loss processes, including natural ferromagnetic resonance and spin relaxation. In addition, interfacial polarization and charge relaxation also support for electromagnetic absorber applications. However, the intrinsic absorption performance of pristine $CoFe_2O_4$ nanoparticles remains limited by imbalance between complex electromagnetic parameters (μ and ε), insufficient impedance matching, and relatively narrow effective absorption bandwidth within practical radar frequency ranges.

In order to overcome these limitations, cationic substituting by trivalent/divalent cation have been widely explored as one of an effective approach to tailor the crystalline structure, and magnetic properties as well as electromagnetic absorber-response of $CoFe_2O_4$ nanoparticles. Partial substitution of divalent and trivalent metal ions, such as Zn^{2+}, Ni^{2+}, Mn^{2+}, Cu^{2+}, and rare-earth ions (La^{3+}, Nd^{3+}, Gd^{3+}), at tetrahedral or octahedral sites of the spinel lattice enables precise control over cation distribution. Thereafter tune their magneto-crystalline anisotropy, saturation magnetization, as well as electrical conductivity especially loss mechanisms. Here, these modifications should directly affect the magnetic resonance frequency, magnetic-dielectric loss intensity, and impedance matching conditions, which are critical factors governing the reflection loss (RL), and effective absorption bandwidth. Modifying the particle size due to partial substitution metal ion will also significantly tune the minimum RL frequency too. In case the electromagnetic-absorber-performance of giga hertz order is desired, the particle size should be tuned below 60 nm [9].

$CoFe_2O_4$ nanoparticles as a microwave absorber has reported owing a RL of –35 dB at a frequency of 10.4 GHz [10], as well as –47.24 dB at a frequency of 9.84 GHz [11]. In the study reported by Gupta *et al*. [12], the total electromagnetic interference (EMI) shielding effectiveness of graphene aerogel was 25.07 dB at a thickness of 5 mm, which was further increased to 42.10 dB with the inclusion of $CoFe_2O_4$ nanoparticles. The incorporation of magnetic $CoFe_2O_4$ not only increased the total EMI shielding of the aerogel but also increased the power absorption from ~37.738% to ~87.788%. Furthermore, incorporating ZnO nanorods along with $CoFe_2O_4$ nanoparticles into the aerogel, the total EMI shielding effectiveness and power absorption were increased to 48.56 dB and ~93.655%, respectively.

Other, in the study reported by Gulzar *et al*. [13], the highest EMI shielding result of 35 dB was achieved in a wide frequency range from 0.1 to 8 GHz using $CoFe_2O_4$. After that, the research conducted by Gill *et al*. [14], the EM shielding behaviour of Polypyrrole-$CoFe_2O_4$-graphene nanocomposites in the X-band (8.2 - 12.4 GHz) was investigated. The shielding effectiveness by absorption (SEA) and reflection (SER) for PCG3 nanocomposites was found to be ~37dB and ~1dB, respectively. Furthermore, according to a study reported by Batoo *et al*. [15], EMI shielding analysis showed an increase in effective shielding (SET) from 11.43 - 12.82 dB using Ba-doped Co-Zn Ferrite. In addition, the research conducted by Li *et al*. [16], hollow microspheres with protrusions/polythiophene at a thickness of 3.0 mm showed a strong electromagnetic dissipation capability (RL = –33.8 dB at 9.5 GHz), with an absorption bandwidth (RL < –10 dB) of 3.1 GHz (8.2 - 11.3 GHz). This opens up the opportunity to study the effects of doping on the performance of electromagnetic absorbers.

Despite reported progress, some limitations in existing studies on Mn- or La-doped $CoFe_2O_4$ remain. The study by Khan and Rehman [17] on Mn^{2+} substitution often resolves the dilemma of unbalanced magnetic and dielectric losses in Mn-doped cobalt ferrite, leading to poor electromagnetic wave absorption. On the other hand, the doping of rare-earth ions La^{3+} often suffers from limited solubility in the spinel lattice due to their large ionic radius, which often results in the formation of a secondary phase whose

exact role in the dual loss mechanism (magnetic and dielectric) remains controversial [18]. Most of the existing studies only focus on the magnitude of magnetic properties in tuning using dopants, so their synergistic effects on high-frequency electromagnetic absorption and effective bandwidth optimization are still less explored.

Various methods have been used to synthesize $CoFe_2O_4$ nanoparticles such as hydrothermal, coprecipitation, sol-gel, and solid-state reaction [19-25]. In this study, the coprecipitation method was preferred to prepare $CoFe_2O_4$ nanoparticles due to its advantages, including a flexible, scalable approach that provides accurate stoichiometric control and uniform nanoparticle fabrication [26]. Manganese and lanthanum cations were chosen to modify their physical characteristics (structural & magnetic properties), including electromagnetic-absorber performance. Finally, the contrasting atomic radii of manganese and lanthanum are expected to exhibit different electromagnetic performance.

Materials and methods

Amount pure analysis chemical used as raw materials were $Co(NO_3)_2.6H_2O$ (Merck, ≥ 99%), $Fe(NO_3)_3.9H_2O$ (Merck, ≥ 99%), $La(NO_3)_3.6H_2O$ (Sigma Aldrich, 99.99%), and $Mn(NO_3)_2.6H_2O$ (Merck, 99.99%) as the sources of precursor. A schematic diagram illustrating the coprecipitation procedure for the preparation of cobalt ferrite as well as Mn- and La-doped cobalt ferrite nanoparticles is shown in **Figure 1**. Firstly, individual chemicals were weighed according to stoichiometry ($CoFe_2O_4$, $Mn_{0.1}Co_{0.9}Fe_2O_4$, and $La_{0.1}CoFe_{1.9}O_4$) and dissolved in 200 mL of distilled water. The solutions were stirred using a magnetic stirrer until homogeneous for 20 min. Separately amount NaOH was dissolved in 100 mL to obtain 4 M using distilled water for titration. Thereafter, the NaOH (Merck, ≥ 99%) solution drop wise to precursor solution while stirrer at 200 rpm and temperature keep constant at 95 °C. After titration, the product precipitated were washed using ethanol and distilled water three times so that the clean product is obtained. Then the obtained product was hydrolyzed in an oven at 100 °C for 12 h. The final products were annealed in a furnace at 400 °C for 5 h at atmospheric condition and following physical characterization.

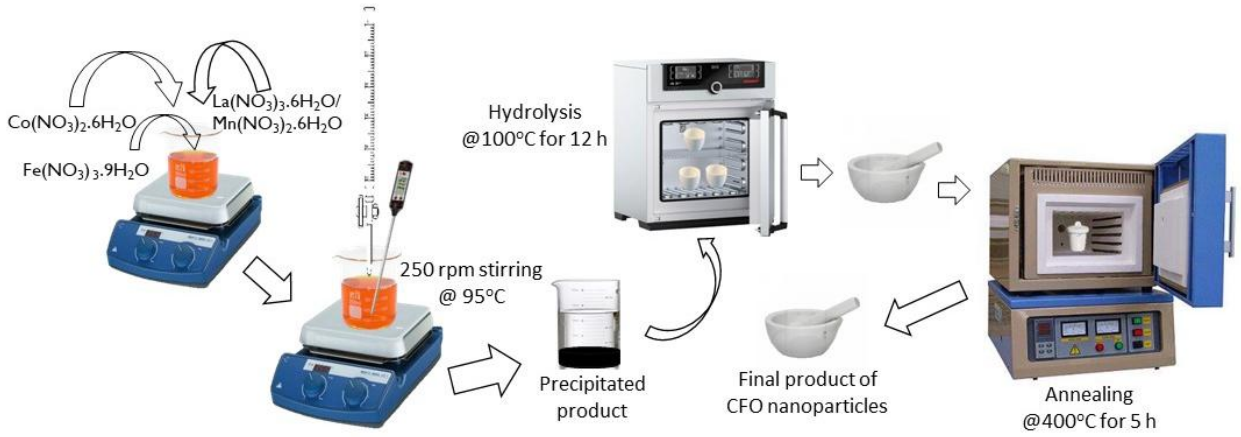


Figure 1 Diagram schematic for the co-precipitation procedure of Mn and La doped $CoFe_2O_4$ nanoparticles.

The samples were then analyzed using a Bruker D8 Advance X-ray diffractometer (XRD) with Cu-Kα radiation (λ = 1.54 Å) to determine their crystalline structure in the 2θ range of 20° - 80°. Utilizing desktop transmission electron microscopy (TEM), morphology was analyzed using ImageJ software, and selected area electron diffraction (SAED) was used to support analysis of the crystal structure. The TEM image of 100 randomly selected granules was used to calculate the particle size distribution. The chemical bonds of the samples were identified with Shimadzu IF Prestige 21 Fourier Transform Infrared (FTIR) spectroscopy in the wavenumber range of 350 - 4,000 cm^{-1}. Meanwhile, the magnetic properties were analyzed via Quantum Design

PPMS VersaLab Vibrating Sample Magnetometer (VSM) at room temperature. Finally, the X-band electromagnetic absorption performance, in the form of reflection loss (RL), was determined using a Vector Network Analyzer (VNA).

Results and discussion

Structural analysis

The diffraction patterns and refinement diffraction patterns of $CoFe_2O_4$ (CFO), Mn-doped $CoFe_2O_4$ (CFO + Mn), and La-doped $CoFe_2O_4$ (CFO + La) are depicted in **Figure 2**. Individual peak in the patterns represents the miller indices of (200), (311), (222), (400), (422), (511), and (440) according to individually 2θ= 30.084°, 35.437°, 37.057°, 43.058°, 53.445°, 56.973°, and 62.585°, respectively, which agreed with ICDD number 221086, confirming the formation of cubic cobalt ferrite with a spinel face-centered cubic (FCC) structure [27]. The calculation of structural parameters (following equations 1-4), i.e., crystallite size (D), crystalline mass density (ρ_x), lattice strain (ε), and the specific surface area (S), is tabulated in **Table 1**. To further confirm the results, Rietveld-refinement analysis was also performed, with the suitability parameters R_{wp}, R_{exp}, R_B, and χ^2 tabulated in **Table 2** (Eqs. (5) - (8)). The chi-square χ^2 calculation, which measures how well the experimental data fit the FCC model with the Fd-3m space group, is further confirmed by the Rietveld refinement findings, which yield values of 1.29, 1.34, and 1.39, all of which are close to the optimal magnitude of 1.0. This finding suggests that the Co^{2+} and Fe^{3+} cations are replaced by Mn^{2+} and La^{3+} doping, or that the sublattices-vacancies-available in the inverse spinel FCC cobalt ferrite structure are occupied.

Calculation of D using the Scherrer equation with the equation at the angle of the strongest peak:

$$\boldsymbol{D = \frac{k\lambda}{\beta \cos\theta}} \quad (1)$$

where D is the crystallite size, k is the Scherrer constant (0.89), λ is the wavelength of X-ray Cu-Kα = 0.15 nm, β is the full width of the diffraction line at half maximum intensity (FWHM) in radians, and θ is the Bragg angle. The ρ_x and ε can be calculated by the following Eqs. [28]:

$$\boldsymbol{\rho_x = \frac{8M}{2a^3}} \quad (2)$$

$$\boldsymbol{\varepsilon = \frac{\beta}{4\tan\theta}} \quad (3)$$

where M is the molecular weight of the sample and a^3 is the cell volume of the sample. Meanwhile, the specific surface area S can be obtained from the relationship between D and ρ_x, namely using the Eq.:

$$\boldsymbol{S = \frac{6}{(\rho_x \times D)}} \quad (4)$$

Rietveld analysis was used to determine the difference in the intensity of the diffraction pattern between the experimental results and calculations, as reflected in the R factor parameters obtained. The R factor is calculated using the Eqs.:

$$\boldsymbol{R_{wp} = 100\left[\frac{\sum_{i=1}^{n} w_i |y_i - y_{c,i}|^2}{\sum_{i=1}^{n} w_i y_i^2}\right]^{\frac{1}{2}}} \quad (5)$$

$$\boldsymbol{R_{exp} = 100\left[\frac{n-p}{\sum_{i=1}^{n} w_i y_i^2}\right]^{\frac{1}{2}}} \quad (6)$$

$$\boldsymbol{R_B = 100\frac{\sum_{i=1}^{n} |I_{obs} - I_{cal}|}{\sum_{i=1}^{n} I_{obs}}} \quad (7)$$

$$\boldsymbol{\chi^2 = \left[\frac{R_{wp}}{R_{exp}}\right]^2} \quad (8)$$

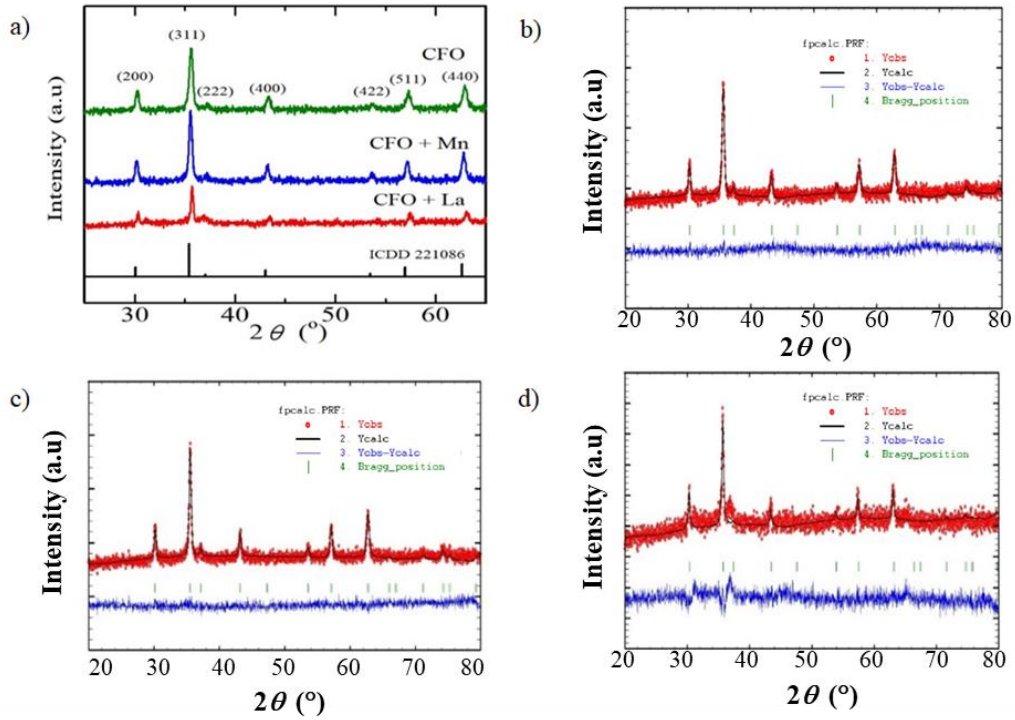


Figure 2 Diffraction patterns of a) Mn/La-doped $CoFe_2O_4$ and refinement diffraction patterns of b) $CoFe_2O_4$, c) Mn-doped $CoFe_2O_4$, d) La-doped $CoFe_2O_4$.

Table 1 Structural parameters of $CoFe_2O_4$, Mn-doped $CoFe_2O_4$, and La-doped $CoFe_2O_4$.

Samples	Parameters			
	***D* (nm)**	**ρ_x (gr.cm^{-3})**	**ε (×10^{-3})**	**S (m^2/g)**
$CoFe_2O_4$	18.13	5.67	6.26	58.40
Mn-doped $CoFe_2O_4$	21.51	5.64	5.28	49.41
La-doped $CoFe_2O_4$	25.47	5.72	4.44	41.19

Rietveld-refinement results confirm that the substitutional doping of Mn^{2+} and La^{3+} did not alter the pristine crystalline structure of cobalt ferrite, as indicated by the lattice parameters, i.e., 8.3686, 8.3788, and 8.3432 Å for the original $CoFe_2O_4$ and both doped samples with Mn^{2+} and La^{3+}, respectively. These findings are also consistent with the results of Rietveld refinement, which revealed lattice parameter values of 8.3589 Å, 8.3739 Å, and 8.3372 Å for $CoFe_2O_4$, Mn-doped $CoFe_2O_4$, and La-doped $CoFe_2O_4$, respectively, as seen in **Table 2**.

In case inverse spinel is considered, cation-doping of divalent Mn^{2+} cations in $Mn_{0.1}Co_{0.9}Fe_2O_4$ is random on both tetrahedral and octahedral sites. Substitution of Mn^{2+} ions into cobalt ferrite causes the movement of Co^{2+} ions from octahedral to tetrahedral sites. Contrary to what is discussed, the trivalent doped La^{3+} cation in $CoLa_{0.1}Fe_{1.9}O_4$ only occupies the octahedral sites [29]. The ionic radii of Fe^{3+}, Co^{2+}, Mn^{2+}, and La^{3+} are 0.65, 0.88, 0.97, and 0.106 nm, respectively [30,31]. The ionic radius of the Mn^{2+} ion is larger than that of Co^{2+}, causing the sublattice on the octahedral site to increase, as well as La^{3+} on the tetrahedral site. Although the larger ionic radii of Mn^{2+} and La^{3+} compared to Co^{2+} and Fe^{3+} induce a local expansion of the host lattice, the expansion alone cannot fully support the observed trends in crystallite size *D*, which increases from 18.13 to 21.51 and 25.47 nm for Mn and La doping, respectively. Rather, this growth behavior is essentially represented in lattice-strain modification and synthesis kinetics. Lattice strain ε is significantly reduced by around 15.65% (= 5.28 - 6.26 / 6.26×100%) for Mn-doping and 29.07% (= 4.44 -

6.26 / 6.26×100%) for La-doping, according to the calculation from Eq. (3). This lattice strain relaxation implies that the inherent microstrain inside the $CoFe_2O_4$ borders is reversibly relieved by the volume expansion (supported by the mass density) brought about by the bigger dopants. Atomic diffusion is facilitated by the reduced strain energy barrier during the treatment temperature/synthesis process, which increases grain boundary mobility and speeds up crystallite formation.

However, Rietveld refinement analysis indicates a parallel decrease in overall crystallinity. This phenomenon can be explained by the synthesis kinetics of rare-earth doping; because La^{3+} is significantly larger than the host ions, its slow diffusion rate into the core spinel lattice tends to accumulate dopants at the grain boundaries. This accumulation generates localized lattice distortions and structural defects, which degrade the long-range crystalline order (lowering crystallinity) despite the larger average crystallite size driven by strain relaxation.

Table 2 Rietveld analysis data of $CoFe_2O_4$, Mn-doped $CoFe_2O_4$, and La-doped $CoFe_2O_4$.

Samples	Parameters					
	R_{wp}	R_{exp}	R_B	χ^2	a (Å)	a_{cal} (Å)
$CoFe_2O_4$	42.50	37.43	17	1.29	8.3589	8.3686
Mn-doped $CoFe_2O_4$	41.60	35.90	13	1.34	8.3739	8.3788
La-doped $CoFe_2O_4$	65.50	55.67	22	1.39	8.3372	8.3432

TEM Results

Figure 3 shows typical TEM, HR-TEM, and SAED images for $CoFe_2O_4$, Mn-doped $CoFe_2O_4$, and La-doped $CoFe_2O_4$. It is clearly observed that for all samples, the TEM profile shows the presence of delicate nano-granular structures. And then it becomes a clear nanoparticle profile for the $CoFe_2O_4$ without and with cation doping (Mn^{2+} and/or La^{3+}) nanoparticles. Meanwhile, the HR-TEM results show adjacent lines indicating the lattice parameters *a*, where the line boundaries denote the distance between repeating lattice points in a unit cell of the samples. HR-TEM measurement of *a* for $CoFe_2O_4$, Mn-doped $CoFe_2O_4$, and La-doped $CoFe_2O_4$ are 8.35, 8.37, and 8.33 Å, respectively. The measurement magnitudes are consistent with the results of XRD calculations, i.e., 8.35(89) Å, 8.37(39) Å, and 8.33(72) Å as well as Rietveld Refinement calculations, i.e., 8.36(86) Å, 8.37(88) Å, and 8.34(32) Å for $CoFe_2O_4$, Mn-doped $CoFe_2O_4$, and La-doped $CoFe_2O_4$, respectively.

Regarding the SAED results of the $CoFe_2O_4$ nanoparticle, the SAED pattern shows sharp and intense concentric diffraction rings. This phenomenon indicates that the $CoFe_2O_4$ nanoparticles are polycrystalline with a small crystallite size. In contrast, for the Mn^{2+} and La^{3+} doped samples, the diffraction profiles appear fainter and more diffuse compared to the case of $CoFe_2O_4$. These results also correlated with XRD analysis, which showed a decrease in crystallinity upon Mn- and La-doping of $CoFe_2O_4$. Furthermore, this pattern in the first case ($CoFe_2O_4$) also indicates lattice strain, as supported by XRD data. The calculated lattice strain Eq. (3) of the $CoFe_2O_4$ sample is 6.26×10^{-3}, which is significantly larger than those of the Mn-doped $CoFe_2O_4$ (5.28×10^{-3}) and La-doped $CoFe_2O_4$ (4.44×10^{-3}) samples, respectively. For all SAED images, the diffraction patterns are thought to originate from the crystallographic planes (200), (311), (222), (400), (422), (511), and (440), which are characteristic of the cubic spinel structure of pure $CoFe_2O_4$ nanoparticles.

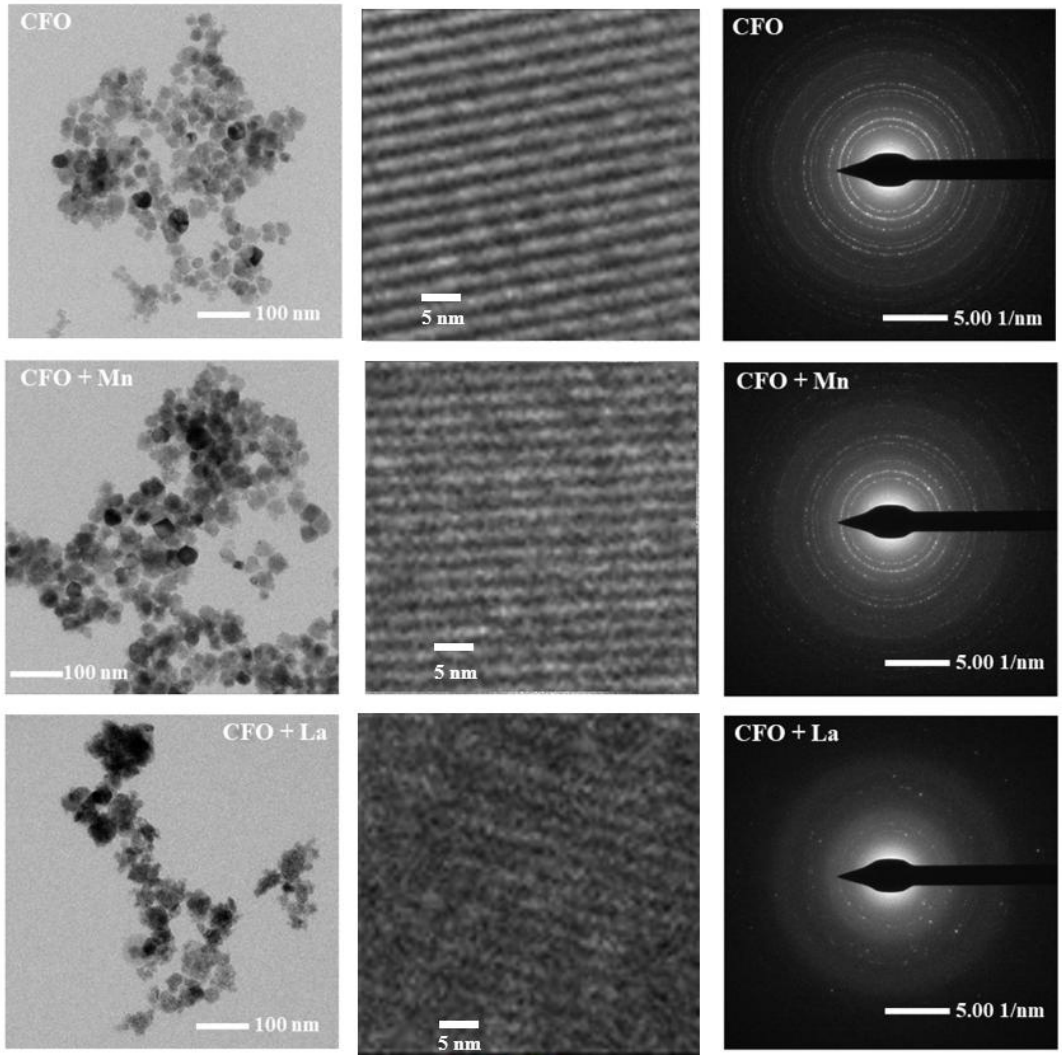


Figure 3 Typical images of TEM, HR-TEM, and SAED of the CFO, CFO + Mn, and CFO + La nanoparticles.

Figure 4 shows the particle size distribution for $CoFe_2O_4$, Mn-doped $CoFe_2O_4$, and La-doped $CoFe_2O_4$ nanoparticles. In the $CoFe_2O_4$ sample, a broader distribution was observed, ranging from ~8 to 28 nm, with a mean of 17.61 nm and a distribution centered around the middle (symmetrical). In contrast, for the Mn-doped $CoFe_2O_4$ sample, the distribution was slightly narrower with a distribution range of ~14 to 32 nm, with a mean of 21.19 nm and a distribution skewed to the left (asymmetrical). In line with that, La-doped $CoFe_2O_4$ also had a narrower distribution than $CoFe_2O_4$, i.e., from ~16 to 34 nm with a mean of 25.34 nm and a distribution skewed to the right (asymmetrical). The obtained data indicate that the substitution of cations with larger ionic radii helps grain growth, resulting in a larger average particle size. The results obtained are also consistent with those of crystallite size calculations based on XRD data.

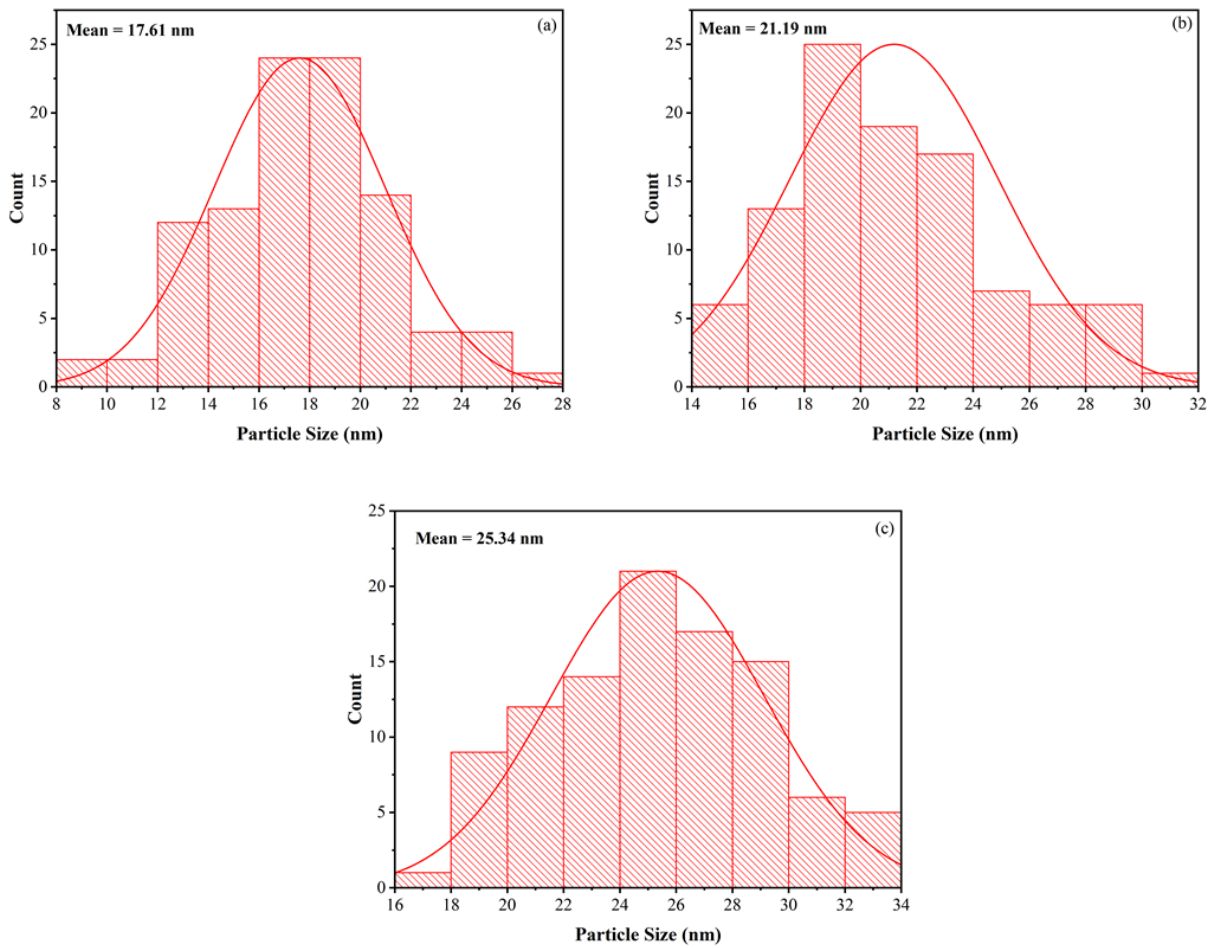


Figure 4 Particle size distribution of (a) $CoFe_2O_4$, (b) Mn-doped $CoFe_2O_4$, and (c) La-doped $CoFe_2O_4$.

FTIR Results

Figure 5 and **Table 3** presents the FTIR spectra of pristine cobalt ferrite (CFO) and Mn- and La-doped CFO samples recorded in the wavenumber range of 400 - 4,000 cm^{-1}. The spectra are used to examine the vibrational characteristics and to verify the formation of the spinel ferrite structure as well as the influence of dopant incorporation.

All samples exhibit 2 prominent absorption bands in the low-frequency region (< 1,000 cm^{-1}), which are characteristic of spinel ferrites. The absorption band located at approximately 550 - 600 cm^{-1} is assigned to the stretching vibration of metal-oxygen bonds at the tetrahedral (A) sites, whereas the band observed around 400 - 450 cm^{-1} corresponds to metal - oxygen vibrations at the octahedral (B) sites. The presence of these bands confirms the successful formation of the cubic spinel structure in all synthesized samples.

For the undoped CFO sample, the vibrational bands are relatively well-defined, indicating a stable metal-oxygen framework (400 - 800 cm^{-1}). Upon Mn and La doping, slight shifts in band positions and variations in band intensities are observed. These changes are directly governed by the alteration of the reduced mass (μ) and the interatomic force constant (k), according to the relation $\left(v \approx \sqrt{\frac{k}{\mu}}\right)$. The substitution of host ions (Co^{2+}/Fe^{3+}) with dopants induces local lattice dynamics modifications via two mechanisms: Mass defect and localized structural strain. For the Mn-doped sample, the subtle shifts stem from minor variations in ionic radii and electronegativity. In contrast, the effect is significantly more pronounced in the La-doped sample. The exceptionally large ionic radius and heavier atomic mass of La^{3+} induce severe local compressive strain, altering the equilibrium metal-oxygen bond lengths and disrupting the orbital hybridization at the structural sites. This strong local lattice distortion fundamentally modifies the bonding strength (k),

resulting in the observed prominent shifts in the vibrational spectra.

A broad absorption band centered around 3,400 cm^{-1} is observed in all spectra and is attributed to the stretching vibration of surface hydroxyl (O–H) groups originating from adsorbed moisture. Additionally, the weak band appearing near 1,600 - 1,650 cm^{-1} corresponds to the bending vibration of molecular water. These features are commonly reported for ferrite nanoparticles and are associated with their high surface-to-volume ratio.

Furthermore, the doped samples exhibit slight band broadening in the low-wavenumber region, suggesting increased lattice disorder and microstructural strain induced by dopant incorporation which is indicated force constant calculation for tetrahedral (k_t) and octahedral (k_o) sites using the following Eqs. (9) - (10) [32]. Such modifications in the metal-oxygen bonding environment are expected to influence the physical properties of cobalt ferrite, including its magnetic and functional performance. Here, the FTIR analysis confirms that Mn and La doping does not alter the fundamental spinel structure of CFO, while effectively modifying the local bonding environment within the lattice.

$$\boldsymbol{k_t = 7.62 \times M_1 \times v_1^2 \times 10^{-7}\ N.m^{-1}} \quad (9)$$

$$\boldsymbol{k_o = 10.62 \times \frac{1}{2} M_2 \times v_2^2 \times 10^{-7}\ N.m^{-1}} \quad (10)$$

with M_1 and M_2 being the molecular weights of the cations at the tetrahedral and octahedral sites. FTIR data can also be used to determine the magnitude of the average force (F) using the Eq. [33]:

$$\boldsymbol{F = \frac{2k_o + k_t}{3}} \quad (11)$$

Furthermore, according to **Table 3**, the v_1 value tended to decrease, i.e., ~0.84% (= (594.10 – 598.92)/598.92×100%, at Mn doping) and ~3.86% (= (575.78 – 598.92)/598.92×100%, at La doping). Furthermore, the v_2 value also decreases, i.e., , i.e., ~1.39% (= (409.89 – 415.68)/415.68×100%, at Mn doping) and ~5.80% (= (391.57 – 415.68)/415.68×100%, at La doping). This decrease is caused by the doping of Mn and La ions into $CoFe_2O_4$, leading to an increase in mass μ and, consequently, a decrease in the force constant. Substitutional doping with Mn^{2+} and La^{3+} ions in cobalt ferrite can modify the force constant at the tetrahedral and octahedral sites, respectively. The force constant plays a role in shifting the core position within the molecule during vibration. **Table 3** presents that the force constants (k_t and k_o) decreased due to substitutional doping with Mn^{2+} and La^{3+}. Substitutional doping with larger ions can increase the radius at the site and reduce the frequency during vibrations at both tetrahedral and octahedral sites [34].

Table 3 Absorption peak (v), force constant (k), average force (F) of $CoFe_2O_4$, Mn-doped $CoFe_2O_4$, and La-doped $CoFe_2O_4$.

Samples	Parameters				
	v_1 (cm^{-1})	v_2 (cm^{-1})	k_t (N/m)	k_0 (N/m)	*F (N/m)*
$CoFe_2O_4$	598.92	415.68	153.48	127.04	135.85
Mn-doped $CoFe_2O_4$	594.10	409.89	151.02	123.53	132.69
La-doped $CoFe_2O_4$	575.78	391.57	141.85	112.73	122.44

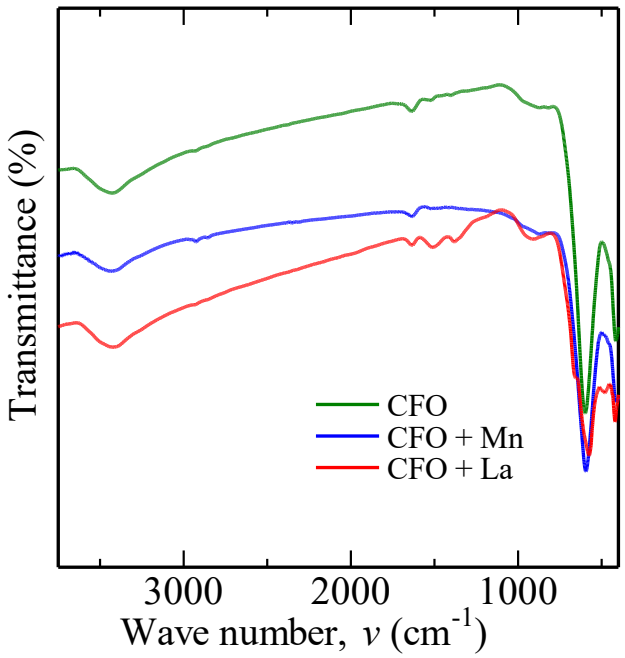


Figure 5 FTIR spectra of $CoFe_2O_4$, Mn-doped $CoFe_2O_4$, and La-doped $CoFe_2O_4$.

Magnetic properties

Figure 6 show the hysteresis curves of $CoFe_2O_4$, Mn-doped $CoFe_2O_4$, and La-doped $CoFe_2O_4$. Meanwhile, **Table 4** presents the parameters of the magnetic properties of $CoFe_2O_4$, Mn-doped $CoFe_2O_4$, and La-doped $CoFe_2O_4$, which explain how the magnetic properties of cobalt ferrite, such as coercivity value (H_C), saturation magnetization (M_S), and remanent magnetization (M_R), can be obtained through the hysteresis curve. The net magnetic moment (n_B) and the magnetic anisotropy constant (K) are calculated using the Eqs.:

$$\boldsymbol{n_B = \frac{M \times Ms}{5585}} \quad (12)$$

$$\boldsymbol{K = \frac{Hc \times Ms}{0.98}} \quad (13)$$

Magnetization in ferrite materials arises from the difference in magnetic moments between the tetrahedral (A-site) and octahedral (B-site) sublattices. The dominant exchange interaction occurs between A and B sites (A–B superexchange via oxygen ions), which aligns the two sublattices antiparallel. As a result, the net magnetization reflects the difference in moment between the two sublattices [35,36]. The relevant ionic magnetic moments are: Fe^{3+} (5 μ_B), Co^{2+} (3 μ_B), Mn^{2+} (5 μ_B), and La^{3+} (0 μ_B, non-magnetic). In the $CoFe_2O_4$ host structure, Fe^{3+} is distributed across both sites, while Co^{2+} preferentially occupies the B-site. Upon Mn^{2+} substitution, the high-spin Mn^{2+} ions (5 μ_B) are expected to occupy B-sites, displacing some Co^{2+} (3 μ_B) and Fe^{3+} ions to the A-site [37]. This cation redistribution increases the net moment at the B-site, thereby enhancing the overall saturation magnetization (M_S) [38]. The magnetic moment (n_B) calculations presented in **Table 4** support this cation redistribution and are consistent with the observed increase in M_S. In contrast, La^{3+} substitution reduces M_S. La^{3+} carries 4f electron spins, which introduce a weak 3d–4f spin coupling that competes with the dominant 3d–3d superexchange interactions governing the magnetic order in $CoFe_2O_4$ [39]. More importantly, La^{3+} is non-magnetic, so its replacement of Fe^{3+} (5 μ_B) at lattice sites directly reduces the net magnetic moment of the system. Together, these effects account for the decline in M_S observed with increasing La^{3+} content.

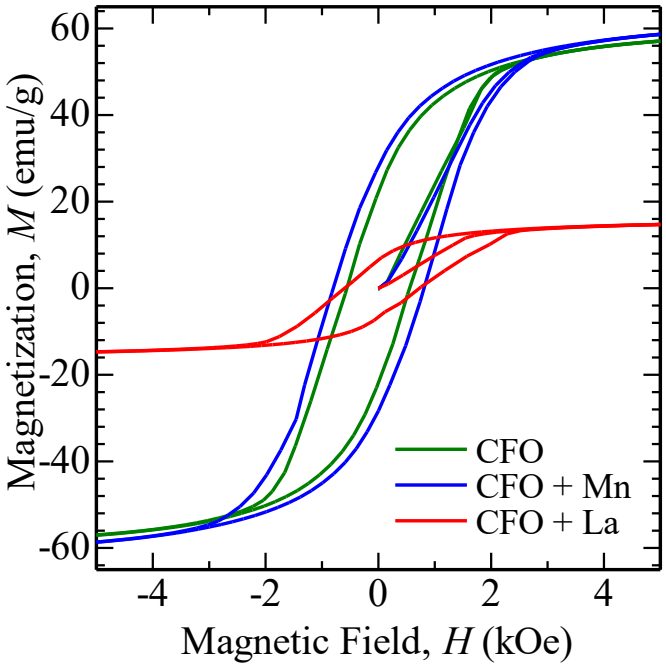


Figure 6 Hysteresis curve of $CoFe_2O_4$, Mn-doped $CoFe_2O_4$, and La-doped $CoFe_2O_4$.

Table 4 Magnetic parameters of $CoFe_2O_4$, Mn-doped $CoFe_2O_4$, and La-doped $CoFe_2O_4$.

Samples	Parameters					
	H_C (Oe)	M_S (emu/g)	M_R (emu/g)	M_R/M_S	n_B (μ_B)	$K\times10^4$ (erg.cm^{-3})
$CoFe_2O_4$	835	52.33	23.78	0.45	2.27	24.39
Mn-doped $CoFe_2O_4$	838	61.10	29.22	0.47	2.65	28.68
La-doped $CoFe_2O_4$	651	13.60	7.14	0.52	0.59	4.92

The coercivity (H_C) trends follow distinct mechanisms depending on the substituent. Mn^{2+} substitution increases H_C, which is attributed to an enhancement of the magnetocrystalline anisotropy constant (K). A higher anisotropy strengthens spin-lattice interactions and promotes domain wall pinning, making magnetization reversal more difficult. Conversely, La^{3+} substitution decreases H_C. The relatively weak magnetic moment of La^{3+}, combined with its tendency to disrupt the periodicity of the crystal lattice, reduces the anisotropy field and facilitates domain wall motion. These trends are consistent with the magnetic anisotropy values reported in **Table 4**, confirming that the nature of the substituting ion plays a decisive role in determining the coercive behavior of the $CoFe_2O_4$ spinel system.

Microwave/Electromagnetic absorption properties

Cobalt ferrite was selected as an electromagnetic absorber material because it has ferrite-based magnetic properties, so it is expected to produce good absorbent properties. The $CoFe_2O_4$, Mn-doped $CoFe_2O_4$, and La-doped $CoFe_2O_4$ samples were molded with a size of 12.5×25×1.5 mm^3 through the hardening process by adding a hardener. This study aimed to determine which sample obtained the expected magnetic properties and performed better in terms of microwave absorbent properties. A VNA test tool was used to determine the microwave absorbent properties conducted at a frequency of 8 - 12 GHz (X band-frequency).

The mechanism of electromagnetic wave absorption occurs due to the resonance frequency between the material and the electromagnetic wave.

This is indicated by the appearance of a reflection loss (RL) peak. The difference in the width of the absorption frequency is likely to come from the resulting permeability value. The magnetic permeability value according to the Eq.:

$$\boldsymbol{\mu = \mu'(real) - j\mu''(imaginary)} \quad (14)$$

From this equation it is explained that the real value of magnetic permeability is energy storage while the imaginary value of magnetic permeability acts as energy loss. The real and imaginary permeability values of the samples are shown in **Figure 7** and the permeability of the two samples has a similar trend and the permeability curves of the Mn-doped $CoFe_2O_4$ and La-doped $CoFe_2O_4$ were in a similar trend. Good microwave absorption properties are always related to the high absorption conditions of an absorber. In general, the absorption rate of a magnetic material is expressed by the magnetic loss tangent tan δ_m as shown in the Eq. [40]:

$$\boldsymbol{tan\,\delta_m = \frac{\mu''}{\mu'}} \quad (15)$$

The absorption properties of a microwave absorber are influenced by the impedance of the absorber. The impedance of the absorber is influenced by the thickness (d), relative permittivity (ε_r), and relative permeability (μ_r). The impedance values that occur in the absorber are shown:

$$\boldsymbol{Z_{in} = Z_0\sqrt{\mu_r/\varepsilon_r}\,tanh^{-1}\left[j\frac{2\pi fd}{c}\sqrt{\mu_r/\varepsilon_r}\right]} \quad (16)$$

The RL values are determined using Eq. [41]:

$$\boldsymbol{RL(dB) = 20log\left|\frac{Z_{in}-Z_0}{Z_{in}+Z_0}\right|} \quad (17)$$

From **Figure 7(a)**, the real permeability μ′ of pure CFO varies approximately from −5.9 to −4.9 over the whole frequency range. This relatively higher μ′ magnitude indicates stronger magnetic energy storage and higher effective magnetization. In contrast, Mn-doped CFO shows lower μ′ values, ranging roughly from −6.5 to −5.6, while La-doped CFO exhibits intermediate magnitudes between −6.3 and −5.4. The reduction in μ′ after doping suggests a decrease in the net magnetic moment, which should be attributed to the cations redistribution between tetrahedral (A) and octahedral (B) sites, as well as to weakened super-exchange interactions (Fe^{3+}–O^{2-}–Fe^{3+}) caused by Mn^{2+}/Mn^{3+} and La^{3+} substitution. Quantitatively, the shift of μ′ toward more negative values and the broader dispersion observed around 9 - 11 GHz indicate enhanced magnetic relaxation processes. The resonance-like minima observed near ~10 - 11 GHz correspond to natural ferromagnetic resonance (FMR), whose position and depth are modified by the dopant species. The deeper minimum in Mn-doped CFO indicates stronger anisotropy field modification and increased spin relaxation.

Figure 7(b) shows that the imaginary permeability μ″, which represents magnetic loss, increases significantly upon doping. The μ″ values for pure CFO remain relatively low (approximately −6 to −5.5), whereas Mn-doped and La-doped CFO reach much higher magnitudes, down to approximately −9.5 and −10.5, respectively, near 10 GHz. This large increase in μ″ quantitatively confirms that doping enhances energy dissipation through magnetic loss mechanisms including domain wall damping as well as eddy current loss. Notably, the La-doped CFO exhibits the highest μ″ magnitude across most of the frequency range, indicating the strongest magnetic loss. This can be explained by the non-magnetic nature of La^{3+} ions, which introduce lattice strain and disrupt long-range magnetic ordering, leading to increased spin disorder and enhanced damping. The higher μ″/μ′ ratio for the doped samples further indicates improved microwave attenuation capability, which is a key requirement for efficient microwave absorbers.

Figure 8 presents the frequency dependence of the magnetic loss tangent (tan δ_m) and reflection loss (RL) of pristine $CoFe_2O_4$ (CFO), Mn-doped CFO, and La-doped CFO in the X-band region (8 - 12 GHz). These results provide direct experimental confirmation of the permeability trends observed in **Figure 7** and demonstrate how dopant-induced changes in μ′ and μ″ translate into microwave absorption performance. As shown in **Figure 8(a)**, the magnetic loss tangent (tan δ_m = μ″/μ′) of all samples exhibits strong frequency dispersion, reflecting the dominance of magnetic relaxation mechanisms in the GHz range. Pristine CFO

shows the lowest tan δ_m values (~1.0 - 1.3), consistent with its relatively low μ″ observed in **Figure 7(b)**. In contrast, both doped samples exhibit significantly enhanced tan δ_m, reaching maximum values of ~1.6 for Mn-doped CFO and ~1.55 for La-doped CFO around 9 - 10 GHz.

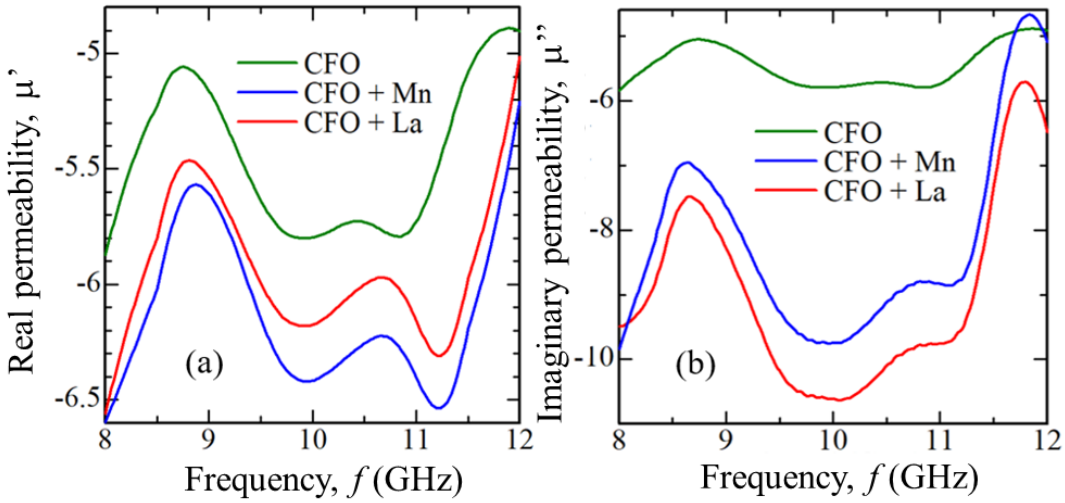


Figure 7 (a) Real and (b) imaginary permeability curves of $CoFe_2O_4$, Mn-doped $CoFe_2O_4$, and La-doped $CoFe_2O_4$.

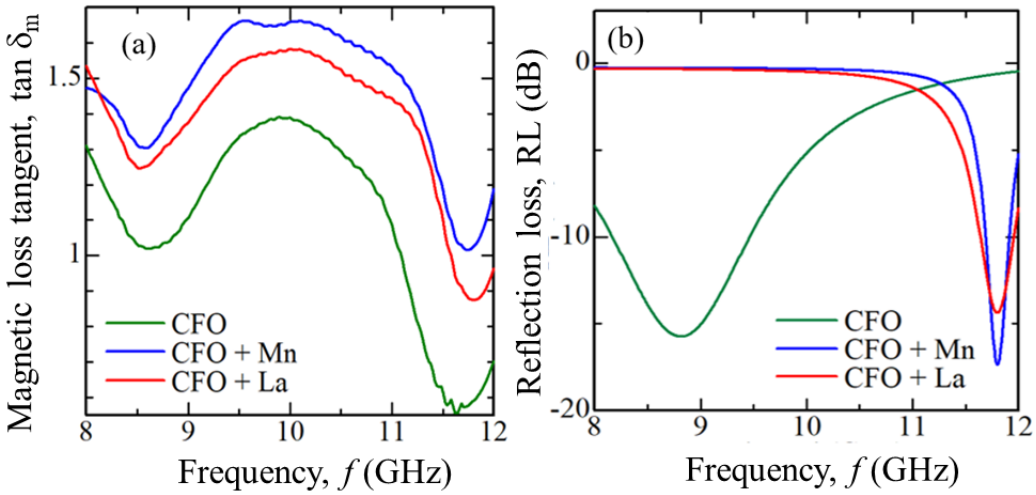


Figure 8 (a) Magnetic loss tangent and (b) reflection loss (RL) of $CoFe_2O_4$, Mn-doped $CoFe_2O_4$, and La-doped $CoFe_2O_4$.

This quantitative enhancement of tan δ_m directly originates from the substantial increase in μ″ induced by cation substitution, as discussed in **Figure 7**. Mn incorporation enhances spin relaxation, while La^{3+} substitution introduces magnetic dilution, which increase damping of spin precession and domain wall motion. The broadened tan δ_m maxima in the doped samples indicate a wider distribution of relaxation times, suggesting the coexistence of natural ferromagnetic resonance and spin-spin relaxation processes. This behavior is characteristic of structurally distorted ferrites and is favorable for broadband microwave attenuation.

Figure 8(b) shows the reflection loss (RL) profiles calculated from the measured complex permittivity and permeability. Pristine CFO exhibits a moderate minimum RL of approximately −13 dB near 9 GHz, corresponding to limited microwave absorption. This is due to insufficient magnetic loss and poor impedance matching. In contrast, Mn- and La-doped CFO display dramatically enhanced absorption performance, with minimum RL values reaching approximately −18 dB (Mn-doped) and −15 dB (La-doped) near 11.5 - 12 GHz.

The shift of the RL minima toward higher frequencies in the doped samples is consistent with the resonance shift observed in μ′ and μ″ in **Figure 7**, confirming that cation substitution effectively tunes the ferromagnetic resonance frequency. The deeper RL minimum of Mn-doped CFO indicates superior impedance matching, which arises from the optimized balance between reduced μ′ and enhanced μ″. Although La-doped CFO exhibits slightly lower RL depth, it shows a broader effective absorption bandwidth, which can be attributed to stronger damping and more distributed loss mechanisms.

Table 5 Reflection loss (RL) of $CoFe_2O_4$, Mn-doped $CoFe_2O_4$, and La-doped $CoFe_2O_4$.

Samples	RL (dB)	Frequency (GHz)
$CoFe_2O_4$	–15.72	8.8
Mn-doped $CoFe_2O_4$	–17.35	11.8
La-doped $CoFe_2O_4$	–14.36	11.8

Conclusions

In summary, the electromagnetic properties and microwave absorption performance of $CoFe_2O_4$ have been effectively tailored through Mn and La cation substitution. The doped samples exhibit a systematic reduction in real permeability and a pronounced enhancement of imaginary permeability, indicating a transition from magnetic energy storage to magnetic energy dissipation. The increased magnetic loss tangent, combined with enhanced dielectric loss originating from interfacial polarization and charge hopping. Consequently, Mn- and La-doped CFO demonstrate markedly improved reflection loss and absorption efficiency in the X-band region, with Mn-doped CFO showing the most balanced performance between loss magnitude and impedance matching, while La-doped CFO offers broader absorption bandwidth due to stronger damping and structural distortion. These results demonstrate that permeability-permittivity co-engineering via cation substitution can enable high-frequency operation of ferrite-based absorbers. The insights presented in this work provide a robust design framework for next-generation microwave absorbing materials and advanced electromagnetic interference shielding applications.

Acknowledgements

This study was financially supported by Direktorat Riset, Teknologi dan Pengabdian kepada Masyarakat, Kementerian Pendidikan, Kebudayaan, Riset dan Teknologi, The Republic of Indonesia, contract number, number 1076.1/UN27.22/PT.01.03/2024.

Declaration of Generative AI in Scientific Writing

The authors acknowledge the use of generative AI tools (Grammarly) in the preparation of this manuscript, specifically for language editing and grammar correction. No content generation or data interpretation was performed by AI. The authors take full responsibility for the content and conclusions of this work.

CRediT Author Statement

Suharno: Conceptualization; Writing - Original Draft. **Ramadona Rahmawati**: Methodology; Formal analysis. **Nurdiyantoro Putra Prasetya**: Formal analysis; Writing - Review & Editing. **Yana Taryana**: Validation; Project administration. **Riyatun**: Resources; Data Curation. **Utari**: Validation; Resources. **Candra Kurniawan**: Formal analysis. **Dede Djuhana**: Supervision. **Terumitsu Tanaka**: Supervision; Validation. **Budi Purnama**: Conceptualization; Funding acquisition; Supervision; Writing - Review & Editing.

References

[1] A Teber and MF Sarac. Cr-substituted nanocrystalline Ni–Co ferrites: Tuning dielectric, magnetic, structural, X band microwave absorption, and characteristic properties. *Journal of Materials Science: Materials in Electronics* 2023; **34**, 290.

[2] P Anil, A Joseph, B Arun, KCJ Raju and VVRK Kumar. Enhanced X-band microwave absorption properties of cobalt ferrite/nitrogen-doped rGO

nanocomposites. *Materials Science and Engineering: B* 2026; **323**, 118859.

[3] X Wang, S Wei, Y Yuan, R Li, Y Wang, Yi Liang, B Wang and C Dong. Effect of copper sulfide nanosphere shell on microstructure and microwave absorption properties of cobalt ferrite/carbon nanotube composites. *Journal of Alloys and Compounds* 2022; **909**, 164676.

[4] S Sahu, RC Gurrala and P Dobbidi. Effect of rare earth substitution on electromagnetic and microwave absorption properties of nickel-cobalt nano ferrite. *Ceramics International* 2023; **49(24)**, 40875-40893.

[5] SM Ansari, A Younis, YD Kolekar and CV Ramana. Cobalt ferrite nanoparticles: The physics, synthesis, properties, and applications. *Applied Physics Reviews* 2025; **12(2)**, 021308.

[6] R Gahlawat and R Shukla. High performance electromagnetic interference shielding in X-band using dysprosium-doped cobalt ferrite–polypyrrole nanocomposites. *Polymer Composites* 2025; **46(18)**, 17184-17200.

[7] CS Joshi, RC Srivastava, A Joshi and HK Verma. Manganese–cobalt ferrite and polyaniline core–shell nanocomposite as an efficient shielding material against electromagnetic interference under X-band frequency. *Polymer Bulletin* 2025; **82**, 1985-2010.

[8] S Manobalan, S Bose and TP Sumangala. Effect of cobalt ferrite concentration on the EMI shielding effectiveness of cobalt ferrite/graphene based epoxy composites. *Polymer Composites* 2024; **45(17)**, 15804-15819.

[9] C Mang, Z Ma, J Luo, M Rao, X Zhang and Z Peng. Electromagnetic wave absorption properties of cobalt-zinc ferrite nanoparticles doped with rare earth elements. *Journal of Rare Earths* 2021; **39(11)**, 1415-1426.

[10] A Johan, D Setiabudidaya, FS Arsyad, Ramlan and WA Adi. Strong and weak ferromagnetic of cobalt ferrite: Structural, magnetic properties and reflection loss characteristic. *Materials Chemistry and Physics* 2023; **295**, 127086.

[11] Y Yuan, S Wei, Y Liang, B Wang and Y Wang. Effect of solvothermal reaction-time on microstructure and microwave absorption properties of cobalt ferrite. *Materials* 2020; **13(23)**, 5331.

[12] S Gupta, SK Sharma, D Pradhan and NH Tai. Ultra-light 3D reduced graphene oxide aerogels decorated with cobalt ferrite and zinc oxide perform excellent electromagnetic interference shielding effectiveness. *Composites Part A: Applied Science and Manufacturing* 2019; **123**, 232-241.

[13] N Gulzar, K Zubair, MF Shakir, M Zahid, Y Nawab and ZA Rehan. Effect on the EMI shielding properties of cobalt ferrites and coal-fly-ash based polymer nanocomposites. *Journal of Superconductivity and Novel Magnetism* 2020; **33**, 3519-3524.

[14] N Gill, AL Sharma, V Gupta, M Tomar, OP Pandey and DP Singh. Enhanced microwave absorption and suppressed reflection of polypyrrole-cobalt ferrite-graphene nanocomposite in X-band. *Journal of Alloys and Compounds* 2019; **797**, 1190-1197.

[15] KM Batoo, M Hadi, R Verma, A Chauhan, R Kumar, M Singh and OM Aldossary. Improved microwave absorption and EMI shielding properties of Ba-doped Co–Zn ferrite. *Ceramics International* 2022; **48(3)**, 3328-3343.

[16] L Li, S Liu and L Lu. Synthesis and significantly enhanced microwave absorption properties of cobalt ferrite hollow microspheres with protrusions/polythiophene composites. *Journal of Alloys and Compounds* 2017; **722**, 158-165.

[17] K Khan and S Rehman. Microwave absorbance properties of zirconium-manganese substituted cobalt nanoferrite as electromagnetic (EM) wave absorbers. *Materials Research Bulletin* 2014; **50**, 454-461.

[18] AA Al-Juaid. La^{3+} substitution impact on structural, magnetic, and electrical properties of $CoFe_2O_4$ synthesized via sucrose auto-combustion. *Materials Research Express* 2023; **10**, 026101.

[19] QY Tamboli, PD Mhase, I Bushnak, AM Alshehri, AG Al-Sehemi, SM Patange and KR Zakde. Eco-friendly sol-gel synthesis and comprehensive analysis of Ruthenium-substituted Cobalt ferrite nanoparticles using Moringa oleifera gum. *Solid State Sciences* 2025; **168**, 108041.

[20] D Marentina, NP Prasetya, Utari, Riyatun,

Suharno, AMT Pradipto, T Surungan and B Purnama. Effect of synthesis temperature on structural, magnetic, and dye removal properties in coprecipitated yttrium-tuned cobalt ferrite nanoparticles. *Journal of Materials Science: Materials in Electronics* 2025; **36**, 1601.

[21] MF Ahmed, A Yasmin, B Biswas, ML Rahman, J Khanam, RJ Rakhi, M Hakim, MS Hossain, F Ahmed, IJ Lithi and N Sharmin. Effect of calcination temperature on nano-cobalt ferrite synthesized by a sol-gel method for modification of its structural, morphological, magnetic, electrical and optical properties. *Materials Advances* 2025; **6(19)**, 6724-6741.

[22] T Ramesh, V Madhavi, PV Rao, K Vagdevi, N Basavegowda and KH Baek. Impact of ultrasonic-assisted co-precipitation synthesis and ultrasonication duration on cobalt ferrite nanostructures: A comparative study of structural, morphological, optical and magnetic properties. *Inorganic Chemistry Communications* 2025; **174(1)**, 114035.

[23] A Saremi, SM Mirkazemi, A Sazvar and H Rezaie. Controlling magnetic and surface properties of cobalt ferrite nanoparticles: A comparison of co-precipitation and solvothermal synthesis methods. *Solid State Sciences* 2024; **148**, 107432.

[24] NM Refat, MY Nassar and SA Sadeek. A controllable one-pot hydrothermal synthesis of spherical cobalt ferrite nanoparticles: Synthesis, characterization, and optical properties. *RSC Advances* 2022; **12(38)**, 25081-25095.

[25] X Qiu, D Ding, S Yang, G Wang, R Chen, M Dzakpasu, P Jin and XC Wang. Solid-state synthesis of cobalt ferrite fitted with γ-Fe2O3-containing nanocage for peroxymonosulfate activation and cobalt leaching control. *Chemical Engineering Journal* 2021; **405**, 126994.

[26] NP Prasetya, D Marentina, Utari, Riyatun and B Purnama. Strain lattice induced magnetism in yttrium substituted cobalt ferrite and their Congo-red dye-removal properties. *Ceramics International* 2025; **51(30)**, 62554-62570.

[27] NP Prasetya, RI Setiyani, Utari, Kusumandari, Y Iriani, J Safani, A Taufiq, NA Wibowo, Suharno and B Purnama. Cation trivalent tune of crystalline structure and magnetic properties in coprecipitated cobalt ferrite nanoparticles. *Materials Research Express* 2023; **10**, 036102.

[28] AK Kole and P Kumbhakar. Cubic-to-hexagonal phase transition and optical properties of chemically synthesized ZnS nanocrystals. *Results in Physics* 2012*;* **2**, 150-155.

[29] FR Mariosi, J Venturini, ADC Viegas and CP Bergmann. Lanthanum-doped spinel cobalt ferrite ($CoFe_2O_4$) nanoparticles for environmental applications. *Ceramics International* 2020; **46(3)**, 2772-2779.

[30] JC Maurya, SV Bhoraskar and VL Mathe. Effect of manganese substitution on magnetoimpedance and magnetostriction of cobalt ferrites. *Physica B: Condensed Matter* 2014; **436**, 220-226.

[31] N Khatun, S Ahmed, MS Hossain, SFU Farhad, M Al- Mamun, MS Alam, MHA Begum, NI Tanvir, M Hakim and S Islam. Influence of Y^{3+} and La^{3+} ions on the structural, magnetic, electrical, and optical properties of cobalt ferrite nanoparticles. *Heliyon* 2023; **9(2)**, 13019.

[32] S Amiri and H Shokrollahi. Magnetic and structural properties of RE doped Co-ferrite (REåNd, Eu, and Gd) nano-particles synthesized by co-precipitation. *Journal of Magnetism and Magnetic Materials* 2013; **345**, 18-23.

[33] JNPK Chintala, S Bharadwaj, MC Varma and GSVRK Choudary. Impact of cobalt substitution on cation distribution and elastic properties of Ni–Zn ferrite investigated by X-ray diffraction, infrared spectroscopy, and Mössbauer spectral analysis. *Journal of Physics and Chemistry of Solids* 2022; **160**, 110298.

[34] M Gul and K Akhtar. Synthesis and characterization of Al-doped manganese ferrite uniform particles for high-frequency applications. *Journal of Alloys and Compounds* 2018; **765**, 1139-1147.

[35] RK Kotnala and J Shah. Ferrite materials: Nano tospintronics regime. *Handbook of Magnetic Materials* 2015; **23**, 291-379.

[36] PI Devi, N Rajkumar, B Renganathan, D Sastikumar and K Ramachandran. Ethanol gas sensing of Mn-doped $CoFe_2O_4$ nanoparticles. *Ieee Sensors Journal* 2011; **11(6)**, 1395-1402.

[37] CC Naik and AV Salker. Fractional substitution of Mn ions in cobalt-copper ferrite: Effect on its

magnetic, dielectric and microstructural properties. *Inorganic Chemistry Communications* 2022; **142**, 109684.

[38] R Jabbar, SH Sabeeh and AM Hameed. Structural, dielectric and magnetic properties of Mn^{+2} doped cobalt ferrite nanoparticles. *Journal of Magnetism and Magnetic Materials* 2020; **494**, 165726.

[39] L Kumar, P Kumar, A Narayan and M Kar. Rietveld analysis of XRD patterns of different sizes of nanocrystalline cobalt ferrite. *International Nano Letters* 2013; **3**, 8.

[40] A Feng, T Hou, Z Jia and G Wu. Synthesis of a hierarchical carbon fiber@cobalt ferrite@manganese dioxide composite and its application as a microwave absorber. *RSC Advances* 2020; **10(18)**, 10510-10518.

[41] M He, K Zhang, H Qiu, H Guo, X Li, Y Guo, Y Zhang and J Gu. Low-frequency microwave absorption composites. *Advanced Science* 2025; **12(35)**, 11580.